Heterogeneous Sensor-based Condition Monitoring in Directed Energy Deposition

Mohammad Montazeri[1], Abdalla R. Nassar[2], Christopher B. Stutzman[2], Prahalada Rao[1*]
[1]Mechanical and Materials Engineering Department
University of Nebraska-Lincoln, Lincoln, NE, 68588-0526 United States
[2]Applied Research Laboratory,
The Pennsylvania State University, University Park, PA 16802, United States

Abstract

The objective of this work is to detect *in situ* the occurrence of lack-of-fusion defects in titanium alloy (Ti-6Al-4V) parts made using directed energy deposition (DED) additive manufacturing (AM). We use data from two types of in-process sensors, namely, a spectrometer and an optical camera which are integrated into an Optomec MR-7 DED machine. Both sensors are focused on capturing the dynamic phenomena around the melt pool region. To detect lack-of-fusion defects, we fuse (combine) the data from the in-process sensors invoking the concept of Kronecker product of graphs. Subsequently, we use the features derived from the graph Kronecker product as inputs to a machine learning algorithm to predict the severity (class or level) of average length of lack-of-fusion defects within a layer, which is obtained from offline X-ray computed tomography of the test parts. We demonstrate that the severity of lack-of-fusion defects is classified with statistical fidelity (F-score) close to 85% for a two-level classification scenario, and approximately 70% for a three-level classification scenario. Accordingly, this work demonstrates the use of heterogeneous in-process sensing and online data analytics for *in situ* detection of defects in DED metal AM process.

Keywords: Directed Energy Deposition; Lack-of-fusion Defects; In-process Optical Emission Spectroscopy; Plume Imaging; Kronecker Graph Product; Sensor Data Fusion.

---

[*] Corresponding author. Email. rao@unl.edu

1 Introduction

1.1 Background and Motivation

Directed energy deposition (DED) additive manufacturing (AM) offers the ability to produce and repair high-value components. The process is also known popularly as Direct Metal Deposition (DMD, a trademark of DM3D), and Laser Engineered Net Shaping (LENS, a trademark of Optomec). However, as currently implemented, the process suffers from a lack of part consistency and quality [1].

Empirical process mapping approaches, such as those utilizing dimensionless numbers to determine the appropriate process parameters to avoid part flaws have been implemented [2, 3]. Nevertheless, such approaches are most appropriate for the DED process under static conditions which produce stable (time-independent) build quality. Unfortunately, seemingly-random defects in DED can occur despite empirical optimization of processing parameters [4]. Such seemingly random, or stochastic flaws, necessitate extensive post-process inspection with X-ray computed tomography (XCT) for quality assurance purposes.

Moreover, XCT is expensive, time-consuming, and becomes progressively less effective with part size and complexity. In-situ identification of defects using sensor signatures offers the promise of reduced inspection cost and increased confidence in part quality. However, sensing and control of DED is complicated by the many material-process-machine interactions involved [5]. For a review of these material-process-machine interactions and strategies to sense and mitigate defects in DED, the reader is referred to one of several works [6-9]. In general, research efforts may be categorized into four groups.

(i) **Melt pool monitoring** chiefly involves measuring the shape, size or temperature of the melt pool, typically, using CMOS or CCD cameras fitted with near infrared (NIR) filter or infrared pyrometers [10-12].

(ii) **Powder delivery rate monitoring**: involves the use of photodiodes and acoustic methods [13] or imaging [14] coupled to the delivery tube [15] or the nozzle [16] to measure the powder flow rates.

(iii) **Layer morphology monitoring** involves assessing the geometry of the deposited layer. For instance, Davim *et al.* projected a line laser is on a deposited layer, the reflection from which is captured using a camera, and subsequently analyzed to ascertain the height of the deposited layer (clad height) [17].

(iv) **Optical emission monitoring**: involves monitoring of optical emission above the melt pool, generated by the highly-excited vapor plume. In laser welding and cladding, the utility of optical emission spectroscopy is well established for process characterization and quality monitoring [18, 19]. More recently, the use of optical emission spectroscopy has been demonstrated for monitoring DED processes [20, 21].

An example of the use of optical emission spectroscopy to monitor the DED process is presented in the work of Song and Mazumder [20], where spectroscopy was used to monitor the elemental composition of chromium-based steel deposits. In a related work, Mazumder *et al.* [22] also use optical spectrometry to identify elemental phase transformation in various powder compositions, including, Iron-Nickel, Iron-Titanium, and Iron-chromium binary powders.

More recently, optical emissions spectroscopy has been applied to measure DED build quality. Nassar *et al.* [21] used a spectrometer, in a setup similar to the one used herein, to identify the onset of lack-of-fusion during DED of Ti-6Al-4V. The experimental results reported by Nassar *et* *al.* show a significant rise in the relative intensities of emissions, corresponding to Titanium lines, relative to the intensity of continuum emissions, in the portions of a part where a non-ideal hatch spacing caused lack-of-fusion defects. Taking this rationale forward, Nassar *et al.* [2] use the line-to-continuum ratio at the 550 nm and 430 nm wavelength regions, derived from the spectrometer as a monitoring statistic to detect defect locations in the part.

Researchers have also recently begun to integrate in-process sensor data with contemporary machine learning approaches to extract patterns and relate sensor data to process conditions and part quality. For instance, Khanzadeh *et al.* [23] investigated the effect of heat affected zone on the emergence of flaws in DED. They demonstrated that by monitoring the features of melt pool images, obtained from functional principal component analysis (FPCA) of dual-wavelength imaging pyrometer data, the onset of lack-of-fusion defects could be predicted through machine learning. A related work by Khanzadeh *et al.* [24] also uses a type of a neural network called self-organizing map to analyze the pyrometer signals and subsequently detect defect locations in DED parts.

1.2 Objective and Hypothesis

The objective of this work is to detect the occurrence of lack-of-fusion defects in the DED of titanium alloy (Ti-6Al-4V) parts by fusing data acquired from multiple in-process sensors. To realize this objective, we develop and apply the concept of Kronecker product of graphs to combine data from two types of sensors: an optical emissions spectrometer and images of the vapor plume obtained from a filtered CCD camera [25, 26]. Three signal features are derived from the sensor data, namely, two line-to-continuum ratio signatures from the spectrometer, and the area of the meltpool plume from the CCD camera. These three features are used in graph-theoretic supervised machine learning, with post-processes XCT data serving as ground truth, to predict defects.

The central hypothesis of this work is that process signatures derived from the graph Kronecker product analysis of the three signal features are statistically significant discriminants of the lack-of-fusion defects that manifest in DED Ti-6Al-4V parts. As a consequence of testing this hypothesis, we show that the severity level of lack-of-fusion defects in a layer is identified with significantly higher statistical fidelity when the signal features derived from the Kronecker graph product approach are used as independent variables, compared to statistical moments-based signal features, such as signal mean and standard deviation. This work thus addresses both the burgeoning need for heterogeneous sensor data fusion and for feature extraction for defect detection in DED.

2 Methods

2.1 Part Build Conditions and Sensor Instrumentation

The salient aspects of the DED process are schematically represented in Figure 1. A stream of powder, aerosolized in an inert carrier gas (typically Argon), is directed onto a substrate via nozzles on a laser processing head. The powder is melted onto the substrate through the thermal action of a laser that is located coaxially with the processing head. By translating the processing head relative to the substrate in the horizontal and vertical planes, the desired part geometry is built layer-upon-layer.

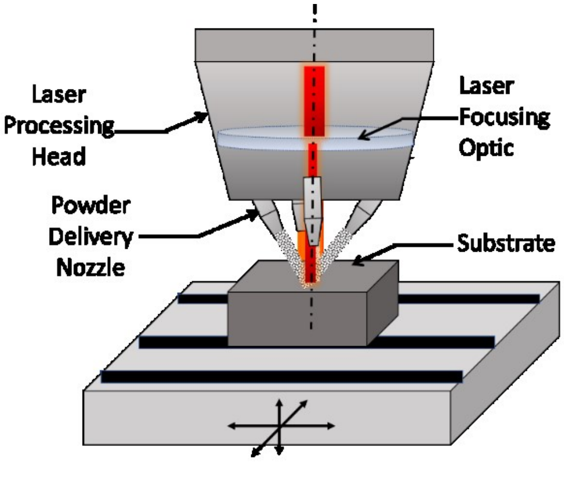

Figure 1: Schematic of the DED process.

This work utilized the data collected by Stutzman, Nassar, and Reutzel described in Ref. [4]. Key experimental details are reiterated here for the convenience of the reader. An Optomec Laser Engineered Net Shaping (LENS) MR-7 DED system is used in this work. In this work, three process parameters were varied: laser power (P, Watt), powder flow rate (F, g/min), and hatch pattern (H, cross, and parallel). The translation speed (10.6 mm/sec), layer height (0.254 mm), and hatch spacing (1 mm) were kept constant. Cuboid-shaped coupons with the dimension of 15 mm × 15 mm × 10 mm (length × width × build height), were built under the ten combinations of DED process parameters settings reported in Figure 2.

These test coupons were built using titanium alloy Ti-6Al-4V powder, with a median powder diameter (D50) of 37.72 µm. Each test coupon is comprised of 40 layers with 12 hatches per layer and is built on a 6.35 mm thick Ti-6Al-4V substrate. A photograph of a representative coupon and an offline XCT slice taken at the second layer for each test coupon are shown in Figure 2. A spectrometer and a CCD camera captured position and time-synchronized data during processing—see Table 1 and Figure 3. The features extracted from the spectrometer signal and plume camera images are the line-to-continuum ratio and total plume area, respectively.

Two line-to-continuum ratios are estimated around wavelengths of 430 nm and 520 nm that corresponds to the emission of atomically-excited titanium (Ti I)[27]. The concept of the line-to-continuum ratio and optical emission spectroscopy for AM applications is explained in recent publications by Nassar *et al.* [4, 21]. The total plume area is calculated after the binarization of the plume images.

Nassar *et al.* in a series of publications have explained implementation details and the physical meaning of the line-to-continuum ratio – i.e., the relationship of the line-to-continuum emission to the elemental excitation of alloy constituents of the powder feedstock, and through it to the quality of the build [4, 21, 28]. Key details are reiterated here for the convenience of the reader. The spectrometer measures the intensity of optical emission at different wavelengths [29]. Titanium makes up close to 90%, by mass, of the composition of Ti-6Al-4V, and exhibits strong, atomically-excited emission lines around 430 nm and 520 nm. Continuum emissions of the plume, meltpool, including blackbody radiations and other extraneous sources are accounted in the rest of the spectrum.

Table 1: Process monitoring sensor information.

Specifications	**Plume Camera**	**Spectrometer**
	Basler Pilot piA640-210gm CCD camera	Ocean optics HR2000+ UV-VIS-IR spectrometer
Locations	152 mm from laser interaction zone inclined at 30° angle relative to the substrate in the vertical plane.	109 mm from laser interaction zone inclined at 20° angle relative to the substrate in the vertical plane.
Detail	Exposure time: 10 ms Frame Rate: 50 Hz	Integration time: 20 ms Wavelength: [200 nm -1100 nm] Slit width: 10 µs Resolution: ~1 nm (FWHM) Optical fiber: 600 µm core diameter

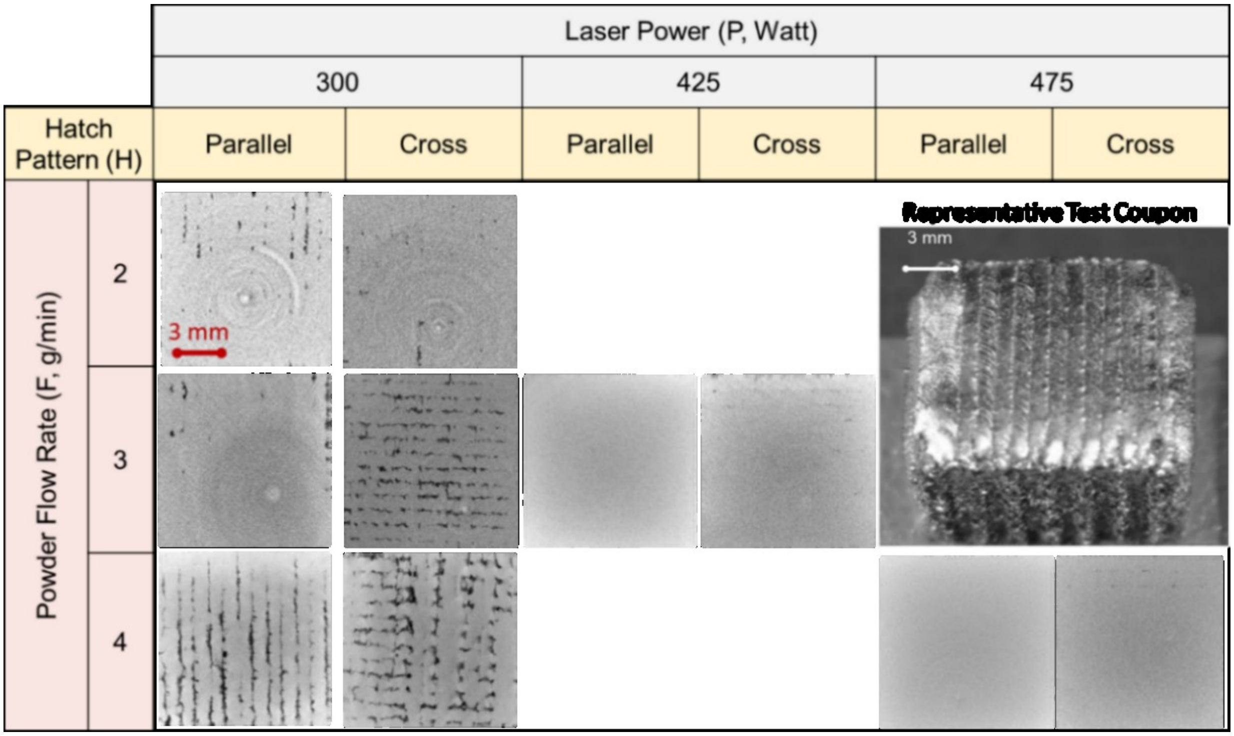

Figure 2: The ten selected printing conditions along with their XCTs related to the second layer.

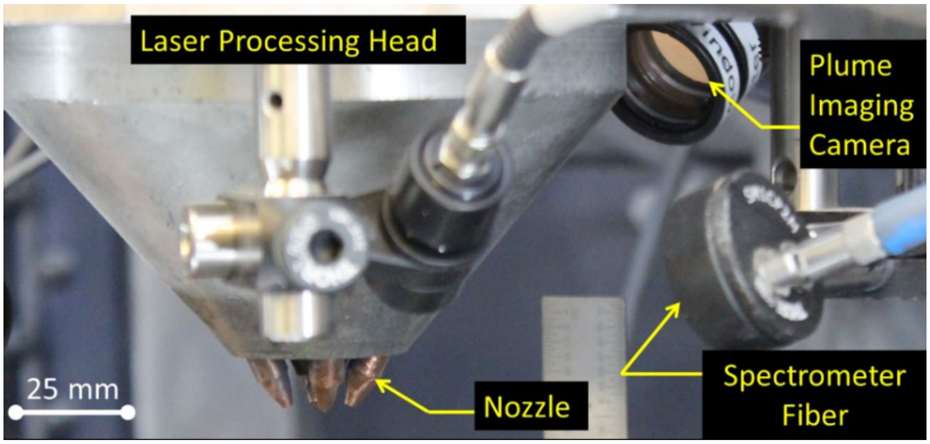

Figure 3: The image of the spectrometer and plume camera integrated into the DED machine.

2.2 Porosity Measurement

Subsequent to deposition, parts were analyzed with X-ray Computed Tomography (XCT) using a voxel size of 15 µm. Image stacks (slices), representing a height of 1 voxel, are extracted from the XCT data along the build direction (z-axis). Each XCT slice is analyzed using four steps, summarized in Figure 4.

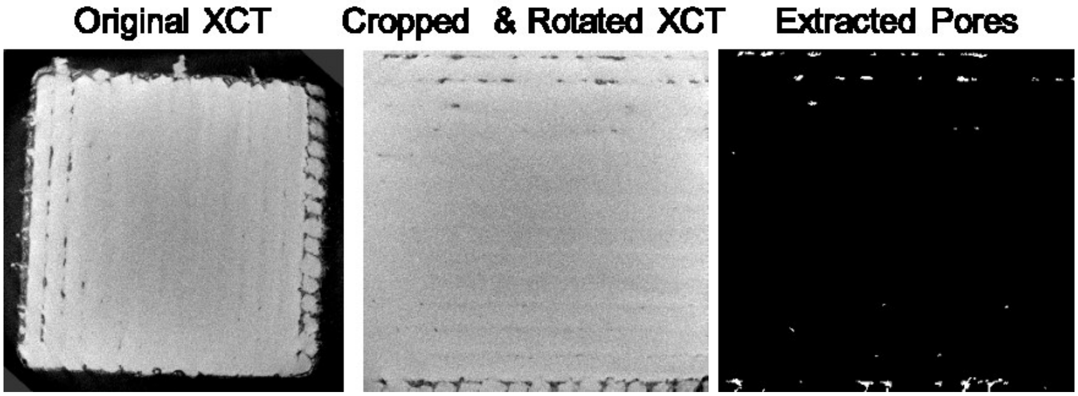

Figure 4: The image processing steps used for extraction of defects characteristics from each XCT slice. The part area is 15 mm × 15 mm.

1. Cropping and rotation of the XCT slices is used to eliminate edge effects and to spatially index the XCT data to the synchronized sensor data, which is in DED machine coordinates.
2. XCT images are converted to black and white (binarized) using a constant threshold value for all images.

3. XCT slices (15 µm thick) are then reduced by projecting slices representing one DED layer (250 µm thick) onto a single plane. This resulted in ~17 XCT slices forming a combined XCT image at each DED layer.
4. Finally, the length of each lack-of-fusion defect on a combined XCT image is determined as the length of the major axis of an ellipse that encompasses the defect.

2.3 Statistical analysis of processing parameters influencing lack-of-fusion porosity

To statistically quantify the effect of process conditions on lack-of-fusion defects, we conduct a generalized linear regression analysis, with the process parameters as inputs and the average length of a lack-of-fusion defect in a layer as output. The three main processing parameter, power (P), powder flow rate (F), and hatch spacing (H), along with their interactions, are assessed to determine if they provide a statically-significant (95% confidence level) determination of average pore length per layer. The regression coefficient (R^2-adj.) is also calculated with and without processing parameter interactions.

2.4 Graph Kronecker product analysis of in-situ sensor data

As an alternative to statistical analysis, which uses the process parameters alone as inputs to predict the average pore length, the main approach presented here is to synthesize data from the spectrometer and plume imaging camera, and subsequently, use the sensor information to detect the level of lack-of-fusion defects in a layer. The approach consists of three steps, as summarized in Figure 5. The first step is to combine data acquired from the spectrometer and plume imaging camera from one layer in the form of a network graph. Following this, the data are analyzed across multiple layers using the concept of Kronecker product of graphs, and thus forming a dictionary of signal patterns. Finally, a machine learning algorithm is trained to predict the average length of lack-of-fusion defects in a layer as a function of the dictionary (input) and tested using a new (unseen) set of sensor data.

The main advantage of the graph Kronecker product approach over traditional statistical signal processing approaches, as will become evident shortly, is that the former encapsulates the inter-relationships between the data obtained at different layers, whereas, the latter considers data from each layer to be independent of preceding and subsequent layers.

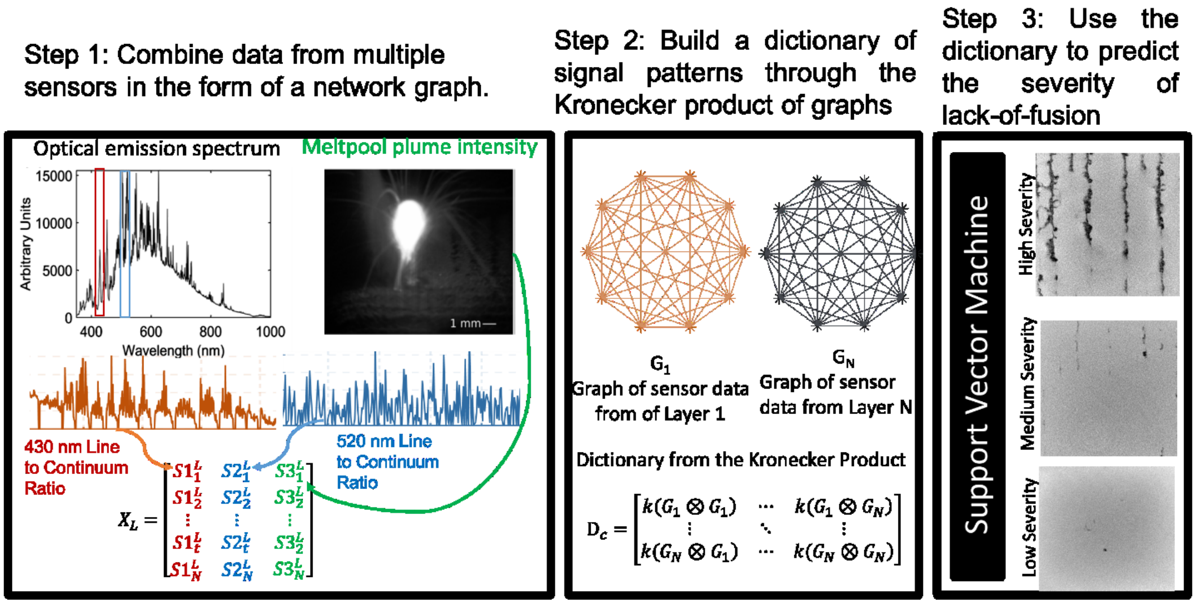

Figure 5: The three steps in the approach to capture data from multiple sensors across layers.

Step 1: Combining the data from multiple sensors into a network graph.

Representative features are extracted from the spectrometer (line-to-continuum ratio around the 430 nm and 520 nm) and meltpool plume camera (the total projected area of the image). Given the different sampling frequencies for the spectrometer and plume camera, the number of data points in line-to-continuum ratios and the plume total area data not identical.

The spectrometer and the plume camera are down-sampled to 30 data points per layer (approximately 15 to 18 individual readings were averaged) to ensure identical data lengths. Labeling the two line-to-continuum measurements at a given instant t in layer L as $S1_t^L$ (430 nm wavelength) and $S2_t^L$ (520 nm wavelength), and the corresponding plume area as $S3_t^L$, the three channels of sensor data for a particular layer (L) can be represented in matrix form X_L as follows:

$$X_L = \begin{bmatrix} S1_1^L & S2_1^L & S3_1^L \\ S1_2^L & S2_2^L & S3_2^L \\ \vdots & \vdots & \vdots \\ S1_t^L & S2_t^L & S3_2^L \\ S1_N^L & S2_N^L & S3_N^L \end{bmatrix}. \tag{1}$$

In matrix X_L, each row is a data point obtained at the time instant *t*, indexed by a sensor along each column. This data is converted into a weighted network graph as discussed in our previous works, and is only briefly described here [30, 31]. The Mahalanobis distance between each row of the data X_L is calculated as follows,

$$w_{ab}^L = (\vec{r}_a^L - \vec{r}_b^L) C^{-1} (\vec{r}_a^L - \vec{r}_b^L)^{\mathrm{T}} \tag{2}$$

Where $\vec{r}_a^L$ and $\vec{r}_b^L$are the *a^th^* and *b^th^* row of the matrix X_L, and C^{-1} is the inverse of the variance-covariance matrix of X_L. The calculated distances using Eqn. (2) will be represented as a matrix G_L.

$$G_L = [w_{ab}^L] \tag{3}$$

The matrix G_L is the weighted, undirected graph representation of the data in layer *L*. The Mahalanobis kernel is used because it normalizes the data.

Step 2: Building a dictionary D_c of graph theoretic features related to the severity level of lack-of-fusion defects.

Given a graph G_L for each layer *L*, every test part can be described as a set of *N* graphs (*N* = 40 layers in this study) through the following Kronecker product random walk kernel [26],

$$\mathrm{D}_c = \begin{bmatrix} k(G_1 \otimes G_1) & \cdots & k(G_1 \otimes G_N) \\ \vdots & \ddots & \vdots \\ k(G_N \otimes G_1) & \cdots & k(G_N \otimes G_N) \end{bmatrix}. \tag{4}$$

The matrix D_c is called the *dictionary* and the subscript *c* refers to the part condition; *c* = {1, 2, …, 10} in this work, since there are 10 process setting combinations. Further, $G_i \otimes G_j$ is the

Kronecker product of graphs G_i and G_j which are representative of the sensors data for layers i and j, respectively, for a particular part. The Kronecker product for matrices X and Y, viz., $X \otimes Y$ is described as:

$$\text{Given, } X = \begin{bmatrix} 1 & 0 & 1 \\ 0 & 0 & 1 \\ 0 & 1 & 0 \end{bmatrix}; \; Y = \begin{bmatrix} 1 & 1 \\ 1 & 0 \end{bmatrix}$$

$$X \otimes Y = \begin{bmatrix} X(1,1).Y & X(1,2).Y & X(1,3).Y \\ X(2,1).Y & X(2,2).Y & X(2,3).Y \\ X(3,1).Y & X(3,2).Y & X(3,3).Y \end{bmatrix} = \begin{bmatrix} 1.\begin{bmatrix} 1 & 1 \\ 1 & 0 \end{bmatrix} & 0.\begin{bmatrix} 1 & 1 \\ 1 & 0 \end{bmatrix} & 1.\begin{bmatrix} 1 & 1 \\ 1 & 0 \end{bmatrix} \\ 0.\begin{bmatrix} 1 & 1 \\ 1 & 0 \end{bmatrix} & 0.\begin{bmatrix} 1 & 1 \\ 1 & 0 \end{bmatrix} & 1.\begin{bmatrix} 1 & 1 \\ 1 & 0 \end{bmatrix} \\ 0.\begin{bmatrix} 1 & 1 \\ 1 & 0 \end{bmatrix} & 1.\begin{bmatrix} 1 & 1 \\ 1 & 0 \end{bmatrix} & 0.\begin{bmatrix} 1 & 1 \\ 1 & 0 \end{bmatrix} \end{bmatrix}$$

$$= \begin{bmatrix} 1 & 1 & 0 & 0 & 1 & 1 \\ 1 & 0 & 0 & 0 & 1 & 0 \\ 0 & 0 & 0 & 0 & 1 & 1 \\ 0 & 0 & 0 & 0 & 1 & 0 \\ 0 & 0 & 1 & 1 & 0 & 0 \\ 0 & 0 & 1 & 0 & 0 & 0 \end{bmatrix}. \tag{5}$$

The random walk kernel, $k(G_i \otimes G_j)$, representative of the similarity between graphs G_i and G_j, is obtained from the Kronecker product $(X \otimes Y)$ as [25],

$$k(G_i \otimes G_j) = \sum_{\substack{\forall \text{rows,} \\ \text{columns}}} \left(\mathrm{I} - \gamma_{ij}(G_i \otimes G_j)\right)^{-1}, \tag{6}$$

where I is the identity matrix and $\gamma_{i,j}$ is the decay constant. The decay constant $\gamma_{i,j}$ is the inverse of the maximal sum taken over the rows (or columns) of $(G_i \otimes G_j)$. In graph theoretic terminology, a random walk encapsulates the number of sequential nodes and edges that need to be traversed to reach a random node B from a starting node A.

A key aspect of the dictionary (D_c) obtained using the Kronecker graph product is that it compares input data from a layer against preceding and subsequent layers, and therefore, captures the inter-dependencies in the data across layers that would be lost if data from each layer is considered independent of other layers as done in statistical signal processing.

Step 3: Training a support vector machine to predict the severity level of the lack-of-fusion flaws based on the dictionary D_c.

Supervised machine learning is used to train a support vector machine (SVM) with a linear discriminant kernel to predict the severity level (low or high) of the lack-of-fusion defects in a layer [32]. The input sensor signals, encapsulated in the dictionary (D_c), are used as input data. We use principal component analysis (PCA) to dimensionally reduce the dictionary D_c, such that only the components representative of 95% variation in the dataset are used as inputs to predict the severity of lack-of-fusion defect in each layer. The PCA procedure convolves all the information in the matrix D_c into a few variables, which makes prediction via machine learning more tractable, stable, and reduces the possibility of over-training.

We have purposely chosen the SVM approach, instead of more sophisticated machine learning models for two reasons. First, in an SVM only a handful of hyper-parameters need to be trained. Second, and more importantly, to support our argument that the features derived from the graph Kronecker product results in higher prediction accuracy compared to statistical features despite using the most rudimentary of machine learning models.

The data against which the inputs are trained is the severity level of lack-of-fusion defects in each layer. This is measured by applying a threshold to the average length of lack-of-fusion defects per layer, derived for the XCT analysis. Two and three-level classification is conducted using threshold values based on XCT analysis—additional discussion of the choice of threshold values is provided in Section 3.1. Low severity of a layer is defined as an average lack-of-fusion flaw size less than or equal to 50 μm. For the two-level classification, high severity was defined as an average lack-of-fusion flaw length greater than 50 μm.

For the three-level classification, the threshold values were 50 µm for low severity, between 50 µm and 200 µm for medium severity, and over 200 µm for high severity. These threshold values were chosen so that there were sufficient number of data points (close to 30) in each class, while perturbation of the threshold does not have any significant effect on the two-level classification scenario, it drastically reduces the data points available for the medium class of severity in the three-level case.

The approach for predicting severity level using unseen input data is as follows. Consider a data stream X_{New} for a new layer identical to the matrix X_L in Eqn. (1), which has not yet been seen by the SVM model. Following the procedure described in Eqn. (2) and (3), we first convert the data X_{new} to the corresponding graph form G_{new}. Next, we obtain the matrix θ_{new} as follows, where G_1 to G_N are the older data already seen by the model.

$$\theta_{new} = [k(G_{new} \otimes G_1) \quad \dots \quad k(G_{new} \otimes G_N)] \tag{7}$$

The input vector in Eqn. (7), θ_{new}, is presented to the *a priori* trained SVM machine learning model after the PCA procedure to obtain the corresponding severity level or class of the lack-of-fusion defects.

The described methods are used to study two cases. The first case in which the machine processing conditions (laser power (P), flow rate (F), and hatch pattern (H), shown in Figure 2 and Figure 6) are assumed to be known and thus included in the machine learning model, and second where the processing conditions are assumed to be unknown and excluded from the machine learning model. In either case the unseen data are later tested following Eqn. (7).

In the first testing scenario, termed the *known process condition* scenario we randomly select sensor data from 30 out of the available 40 layers from each of the 10 test parts to train the corresponding dictionary, D_c, (30×30 matrix) for each part using Eqn. (4). The unseen 10 layers in each of the 10 parts are later used for testing. This implies there is sensor signature and corresponding porosity data from 100 layers (= 10 parts × 10 layers) available for testing. In the second case, called the *unknown process conditions* scenario, the dictionary D_c (300×300 matrix) is built based on the random sampling of 300 layers from the data available from all of the 10 test parts (each part has 40 layers, hence there are 400 layers to sample). As in the previous case, once again we quarantine sensor signatures and porosity data from 100 layers for testing purposes.

Testing results are provided in the form of the confusion matrix shown in Table 2 and using the Precision, Recall, and F-score values calculated using Eqn. (8). This training and testing procedure are repeated five times (5-fold validation procedure), and the average F-score over the training data set is reported.

Table 2: Classification outputs and measures arranged in the form of a confusion matrix.

	Predicted Classes	
True Classes ↓	Predicted Condition Positive	Predicted Condition Negative
True Condition Positive	True Positive	False Positive (Type I error)
True Condition Negative	False Negative (Type II error)	True Negative

$$\begin{aligned} \text{Precision} &= \frac{\text{Number of True Positives}}{\sum \text{Predicted Condition Positive}} \\ \text{Recall} &= \frac{\text{Number of True Positives}}{\sum \text{True Condition Positive}} \\ \text{Fscore} &= 2 * \frac{\text{Precision} \,.\, \text{Recall}}{\text{Precision} + \text{Recall}} \end{aligned} \tag{8}$$

3

3 Results and Discussion

This section is divided into two parts. In Sec. 3.1 we analyze the statistical significance of three process parameters, namely: laser power (P, Watt), powder flow rate (F, g/min), and hatch pattern (H, cross vs. parallel) on the average length of lack-of-fusion defect in each layer. In Sec. 3.2, we use the graph Kronecker analysis of the in-process sensor, to predict the severity level of the lack-of-fusion defects per layer.

3.1 Offline Statistical Analysis of Lack-of-fusion Defect Characteristics from XCT Slices

Aggregated values for the average length of lack-of-fusion defects across all 40 layers for each test parts used in this work are provided in Table 3. Three out of ten samples have an average lack-of-fusion length, across all layers, less than 50 μm. Qualitative XCT analysis of these samples reveals low flaw severity. Another three samples contain an average lack-of-fusion flaw length between 50 μm and 200 μm—these are categorized as having medium flaw severity. All other samples have high flaw severity. These severity levels demarcated based on average pore length are used in Section 3.2 for two- and three-level classification of each layer.

Table 3: Printing conditions of 10 parts and their estimated average pore length (descending order).

Laser Power [W]	Powder Feed Rate [g/min]	Hatch Pattern	Average length of lack-of-fusion defects in a layer [μm]	Two-level Classification State	Three-level Classification State
300	4	Parallel	302	High Severity	High Severity
300	3	Parallel	294	High Severity	High Severity
300	3	Cross	235	High Severity	High Severity
300	2	Parallel	213	High Severity	High Severity
300	4	Cross	189	High Severity	Medium Severity
300	2	Cross	165	High Severity	Medium Severity
475	4	Cross	70	High Severity	Medium Severity
425	3	Cross	39	Low Severity	Low Severity
425	3	Parallel	34	Low Severity	Low Severity
475	4	Parallel	26	Low Severity	Low Severity

The effect of the three process parameters, power (P), powder flow rate (F), and hatch pattern (H) on the average length of lack-of-fusion defect in a layer is shown in Figure 6. Generalized linear regression analysis indicates that P, F, and H along with the interactions P × H and P × F are statistically significant determinants of the aggregated average pore length of all layers of a build. However, the linear regression coefficient (R^2-adj.) was only 47% with main and interaction terms included and 42% with only main P, F, and H. In other words, if the process parameters are the sole predictors of the average length of lack-of-fusion defect in a layer, the fidelity of the prediction would be less than 50%. Accordingly, there is a need to augment the process parameters with in-process sensor signatures to predict pore formation in DED.

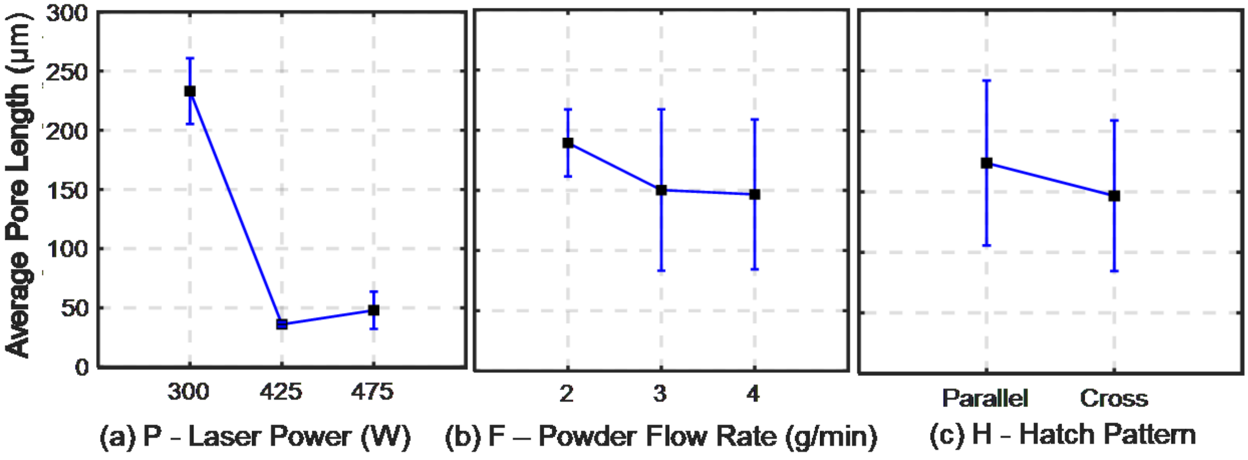

Figure 6: Individual plots representing the effect of each process parameters (a) laser power, (b) powder flow rate, (c) and hatch pattern. The error bars represent a variation of one standard deviation.

Qualitative differences in the line-to-continuum and total plume area data are observed across layers of varying degrees of lack-of-fusion. This is illustrated in Figure 7, where histograms (empirical probability distributions) of the line-to-continuum ratio at 520 nm and the total plume area are provided for three layers, of the same build, with varying severity of lack-of-fusion. While subtle distinction in the shape of the empirical probability distribution are evident in Figure 6(a) and (b), quantification of these differences is challenging; thus, no attempt at a purely statistical correlation of sensor data to flaw severity is made.

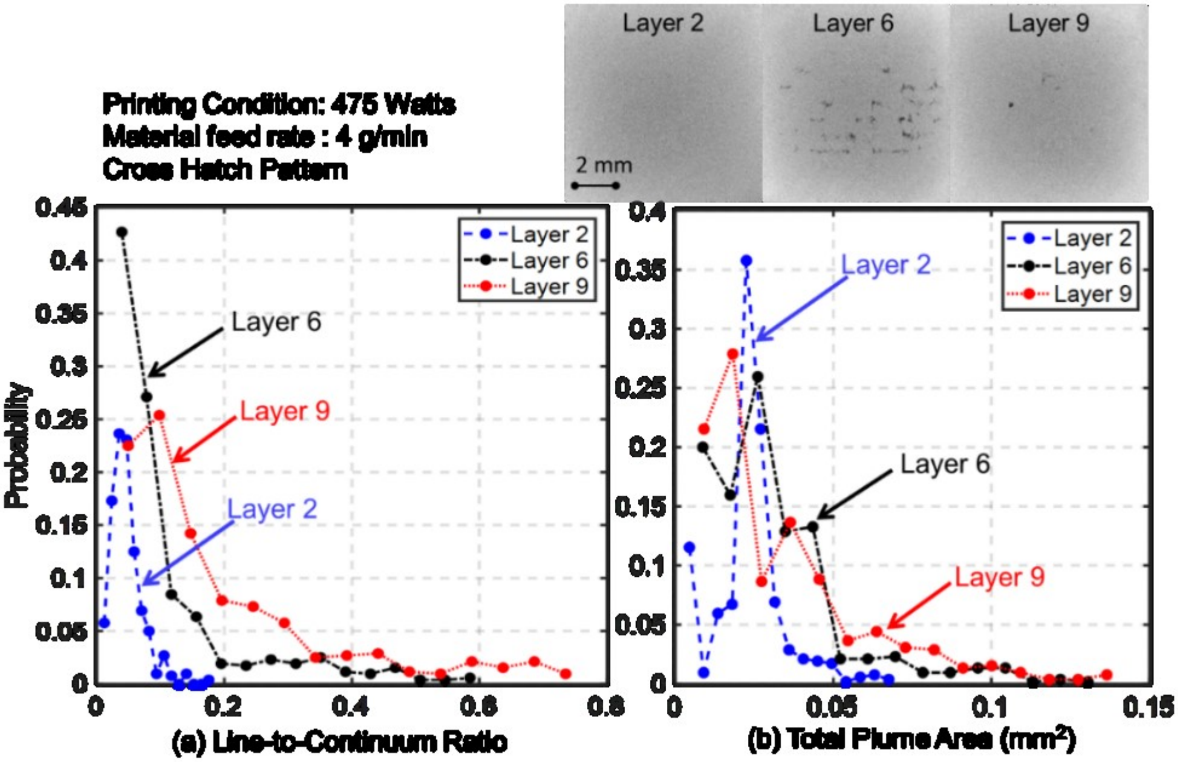

Figure 7: (a) the discrete probability distributions of the (a) line-to-continuum ratio and (b) total plume area, all are related to three different layers when the printing conditions set at laser power = 475 W, flow rate = 4 g/min, and hatch pattern is of the cross-type.

More pertinently, we note that while the overall quality of the 10 parts shown in Table 3 are labeled based on the average length of lack-of-fusion defects, however, Figure 7 shows that the defects can be different in different layers even with the same part. Accordingly, in this work, the layers in a part are not labeled in the same category as that of the part they belong to in Table 3. Instead, the pore severity of each layer is individually labeled as belonging to a particular category through measurement of pore length from XCT slices as described in Sec. 2.2 independent of the label of the part from which the layer originates.

3.2 Online detection of lack-of-fusion defects using sensor data

Results for the two training scenarios tested, known process condition and unknown process conditions are presented in the confusion matrix in Table 4. From Table 4(a), it is evident that treating the process conditions as known leads to a higher classification fidelity compared to the scenario where the process conditions are unknown (Table 4(b)).

Further examination of the confusion matrix in the known process condition scenario reveals that classifying the average pore length into two levels is accomplished with greater statistical fidelity compared to the three-level case.

Table 4(a): Representative confusion Matrix for detection of lack-of-fusion defects stratified into two-level and three-levels of severity with graph random-walk technique assuming process conditions are **known**. (X refers to average length of the lack-of-fusion defect per layer).

Confusion Matrix for two-Level Classification (known process condition)

True Classes ↓	Predicted Classes	
	Low Severity (X < 50 µm)	*High Severity* (X > 50 µm)
Low Severity	20 (out of 26)	6 (False Alarm)
High Severity	12 (Failing to detect)	62 (out of 74)

Confusion Matrix for Three-Level Classification (known process condition)

True Classes ↓	Predicted Classes		
	Low Severity (X < 50 µm)	*Medium Severity* (50 µm < X < 200 µm)	*High Severity* (X > 200 µm)
Low Severity	20 (out of 26)	0	6
Medium Severity	4	21 (out of 37)	12
High Severity	6	9	22 (out of 37)

Table 4(b): Confusion Matrix for detection of lack-of-fusion defects stratified into two-level and three-levels of severity with graph random-walk technique assuming process conditions are **unknown**. (X refers to average length of the lack-of-fusion defect per layer).

Confusion Matrix for two-Level Classification (unknown process conditions)

True Classes ↓	Predicted Classes	
	Low Severity (X < 50 µm)	*High Severity* (X > 50 µm)
Low Severity	2 (out of 34)	32 (False Alarm)
High Severity	7 (Failing to detect)	59 (out of 66)

Confusion Matrix for Three-Level Classification (unknown process conditions)

True Classes ↓	Predicted Classes		
	Low Severity (X < 50 µm)	*Medium Severity* (50 µm < X < 200 µm)	*High Severity* (X > 200 µm)
Low Severity	5 (out of 34)	0	29
Medium Severity	3	0 (out of 34)	31
High Severity	5	0	27 (out of 32)

In Table 5 the statistical fidelity of classification for the two scenarios is expressed in terms of the F-score, which captures both the Type I and Type II statistical errors (a higher F-score is desirable). For the known process condition scenario, the two-level classification fidelity in terms of the F-score is ≈ 85% compared to ≈70% for the three-level case. The results from Table 5 indicate that the prediction accuracy using the input sensor data or process parameters alone is poor, but when the sensor data and process information are combined together, the predictive power of the approach is substantially improved (almost doubled).

Moreover, prediction fidelity (F-score) does not improve when more than one sensor is used in the Kronecker graph product analysis. This is reasonable considering that all the sensors used in this work are focused on the acquisition of data from the meltpool plume region, and hence, capture the same phenomena [4]. The effectiveness of the sensor fusion approach could potentially be magnified with multi-phenomena sensing.

Table 5: Performance of the graph classification approach (F-score) in comparison with the statistical features for discriminating between 2-level and 3-levels of lack-of-fusion severity. The numbers in the parenthesis is the standard deviation from a 5-fold cross-validation study.

Input Data		2-level F Score (%)		3-level F Score (%)	
		Conditions Known	Conditions unknown	Conditions Known	Conditions unknown
Graph Kronecker Product	Line-to-Continuum Ratio (430 nm)	84.8 (8.0)	40.0 (1.0)	72.4 (2.5)	23.4 (5.7)
	Line-to-Continuum Ratio (520 nm)	86.4 (5.2)	41.0 (3.3)	72.2 (2.8)	26.9 (6.9)
	Plume Imaging Sensor	85.4 (9.5)	40.0 (1.0)	71.4 (6.2)	30.3 (3.7)
	All Sensors	84.6 (6.3)	43.6 (4.6)	71.5 (3.9)	21.2 (3.1)
Principal Components of Statistical Features (with all sensors)		40.3 (1.0)		37.3 (2.5)	
Raw Statistical Features (18 features total with all sensors)		87.9 (3.0)		69.4 (3.3)	

An obvious question is whether the Kronecker graph product approach is worth the complexity of implementation—why not just use statistical features and inputs to the machine learning method? To address this, we repeat our analysis using only statistical features (instead of the graph theoretic features). Input features included the mean, standard deviation, range, skewness, kurtosis, and interquartile range from the two line-to-continuum ratio data streams from the spectrometer, as well as the plume image as features, for a total of 18 features (6 features from each signal).

Further, the statistical features are subjected to the PCA procedure, and to ensure equitable comparison with the Kronecker graph product approach, the number of components that captured 95% of the variation are used. The results from the Kronecker graph features and statistical features after PCA are juxtaposed in Table 5. As shown in Table 5, the graph-theoretic Kronecker product features extracted from sensor signatures lead to a much better prediction of part quality, with an F-score nearly double of that when using the traditional statistical features, in both the two-level and three-level classification cases, thus validating our approach.

Lastly, we cross-verified the graph Kronecker product results against those obtained using eighteen raw statistical features, without PCA reduction, as inputs to the SVM model. The raw statistical features showed accuracy comparable to the graph Kronecker product, which uses only two input features, for both two- and three-level classification. However, the fact that 18 statistical features are required to reach a similar F-score as the graph Kronecker product, which has only two features from principal components once again demonstrates the advantage of the Kronecker product approach. Additionally, using such a large number of statistical features makes a machine learning model susceptible to overfitting.

We note that the F-score results from applying the PCA procedure to the raw statistical features are significantly inferior to those obtained using the raw statistical features alone (last two rows of Table 5). This is probably because of two inherent limitations in the PCA procedure. First, PCA tends to neutralize the effect of outliers as it scales each feature based on its corresponding mean value taken over all data points. Since layers with flaws tend to have signal features values that cluster significantly away than the mean, the information concerning layers with flaws may be lost. Second, the PCA is a linear dimension reduction technique which is most effective when the underlying signal distribution and signal noise are both Gaussian, however, as evident from Figure 7, the line-to-continuum ratio and total plume area signatures are both distinctly non-Gaussian [33].

4 Conclusions and Future Work

This work developed and applied a new Kronecker graph product approach for combining data from multiple sensors to detect the onset of defects related to insufficient material fusion (lack-of-fusion defects) in DED AM processing of titanium alloy (Ti-6Al-4V) parts. Three channels of in-process sensor data were acquired during the build: two channels of line-to-continuum optical emission obtained around 430 nm and 520 nm wavelengths and the total area of the plume area from a CCD camera filtered at 430 nm. X-ray computed tomography (XCT) data were used as ground truth to train machine learning algorithms to predict the severity (class or level) of the average length of lack-of-fusion defects within a layer. A limitation of this approach is that only flaws observed within the XCT data (limited to a voxel size of 15 microns) can be used for training and testing. Specific outcomes from this work are enumerated as follows.

1. The effect laser power, powder flow rate, and hatch pattern on the average pore length was quantified. All have a statistically significant effect on the average pore length, with the laser power having the largest effect.
2. Using a Kronecker product analysis of input sensor data together with support vector machine, we demonstrate prediction of the severity of lack-of-fusion defects across a layer with statistical fidelity (F-score) approaching 75% to 85% . In comparison, the traditional statistical-feature-based machine learning approach had a corresponding fidelity of 35% to 40%.
3. Information obtained from both sensor data and process parameters are necessary to obtain statistically viable accuracy (above chance).

This work lays the foundation for a *qualify-as-you-build* framework in AM processes, whereby defects are identified before the next layer is deposited, thus allowing corrective action. In the forthcoming work, we will analyze the statistical fidelity of the approach in detecting different types of defects given data from heterogeneous sensors.

Acknowledgements

Funding at The Pennsylvania State University: This work uses data collected at the Applied Research Laboratory at the Pennsylvania State University under programs supported by the Office of Naval Research, under Contract No. N00014-11-1-0668 and Air Force Research Laboratory through America Makes under agreement number FA8650-12-2-7230. Any opinions, findings and conclusions or recommendations expressed in this publication are those of the authors and do not necessarily reflect the views of the Office of Naval Research, Air Force Research Laboratory, or America Makes.

Funding at the University of Nebraska-Lincoln: One of the authors (PKR) thanks the National Science Foundation for funding his research through the following grants CMMI-1719388, CMMI-1739696 and CMMI-1752069 (CAREER) at University of Nebraska-Lincoln. Specifically, the concept of using spectral graph theory for modeling and monitoring in metal additive manufacturing applications was funded through CMMI-1752069 towards a *correct-as-you-build* smart additive manufacturing paradigm.

References

[1] Huang, Y., Leu, M. C., Mazumder, J., and Donmez, A., 2015, "Additive Manufacturing: Current State, Future Potential, Gaps and Needs, and Recommendations," Journal of Manufacturing Science and Engineering, 137(1), pp. 014001-014001-014010.doi:10.1115/1.4028725

[2] Mukherjee, T., Manvatkar, V., De, A., and DebRoy, T., 2017, "Dimensionless numbers in additive manufacturing," Journal of Applied Physics, 121(6), p. 064904.doi:10.1063/1.4976006

[3] King, W. E., Barth, H. D., Castillo, V. M., Gallegos, G. F., Gibbs, J. W., Hahn, D. E., Kamath, C., and Rubenchik, A. M., 2014, "Observation of keyhole-mode laser melting in laser powder-bed fusion additive manufacturing," Journal of Materials Processing Technology, 214(12), pp. 2915-2925.doi:https://doi.org/10.1016/j.jmatprotec.2014.06.005

[4] Stutzman, C. B., Nassar, A. R., and Reutzel, E. W., 2018, "Multi-sensor investigations of optical emissions and their relations to directed energy deposition processes and quality," Additive Manufacturing, 21, pp. 333-339

[5] Vetter, P. A., Engel, T., and Fontaine, J., 1994, "Laser cladding: the relevant parameters for process control," Laser Materials Processing: Industrial and Microelectronics Applications, SPIE Europto High Power Lasers and Laser Applications Conference, Vienna, Austria, pp. 452-462

[6] Thompson, S. M., Bian, L., Shamsaei, N., and Yadollahi, A., 2015, "An overview of Direct Laser Deposition for additive manufacturing; Part I: Transport phenomena, modeling and diagnostics," Additive Manufacturing, 8, pp. 36-62.doi:https://doi.org/10.1016/j.addma.2015.07.001

[7] Shamsaei, N., Yadollahi, A., Bian, L., and Thompson, S. M., 2015, "An overview of Direct Laser Deposition for additive manufacturing; Part II: Mechanical behavior, process parameter optimization and control," Additive Manufacturing, 8, pp. 12-35.doi:https://doi.org/10.1016/j.addma.2015.07.002

[8] Nassar, A. R., and Reutzel, E. W., 2015, "A survey of sensing and control systems for machine and process monitoring of directed-energy, metal-based additive manufacturing," Rapid Prototyping Journal, 21(2), pp. 159-167.doi:10.1108/RPJ-12-2014-0177

[9] Tapia, G., and Elwany, A., 2014, "A Review on Process Monitoring and Control in Metal-Based Additive Manufacturing," Journal of Manufacturing Science and Engineering, 136(6), pp. 060801-060801-060810.doi:10.1115/1.4028540

[10] Song, L., Bagavath-Singh, V., Dutta, B., and Mazumder, J., 2012, "Control of melt pool temperature and deposition height during direct metal deposition process," The International Journal of Advanced Manufacturing Technology, 58(1), pp. 247-256.doi:10.1007/s00170-011-3395-2

[11] Song, L., and Mazumder, J., 2011, "Feedback Control of Melt Pool Temperature During Laser Cladding Process," IEEE Transactions on Control Systems Technology, 19(6), pp. 1349-1356.doi:10.1109/TCST.2010.2093901

[12] Bi, G., Gasser, A., Wissenbach, K., Drenker, A., and Poprawe, R., 2006, "Identification and qualification of temperature signal for monitoring and control in laser cladding," Optics and Lasers in Engineering, 44(12), pp. 1348-1359.doi:https://doi.org/10.1016/j.optlaseng.2006.01.009

[13] Whiting, J., Springer, A., and Sciammarella, F., 2018, "Real-time acoustic emission monitoring of powder mass flow rate for directed energy deposition," Additive Manufacturing, 23, pp. 312-318.doi:10.1016/j.addma.2018.08.015

[14] Kriczky, D. A., Irwin, J., Reutzel, E. W., Michaleris, P., Nassar, A. R., and Craig, J., 2015, "3D spatial reconstruction of thermal characteristics in directed energy deposition through optical thermal imaging," Journal of Materials Processing Technology, 221, pp. 172-186.doi:10.1016/j.jmatprotec.2015.02.021

[15] Hu, D., and Kovacevic, R., 2003, "Sensing, modeling and control for laser-based additive manufacturing," International Journal of Machine Tools and Manufacture, 43(1), pp. 51-60.doi:http://dx.doi.org/10.1016/S0890-6955(02)00163-3

[16] Boddu, M. R., Landers, R. G., Musti, S., Agarwal, S., Ruan, J., and Liou, F. W., 2003, "System Integration and Real-Time Control Architecture of a Laser Aided Manufacturing Process," Solid Freeform Fabrication Symposium, Austin, Texas, pp. 522-530

[17] Davim, J. P., Oliveira, C., Cardoso, A., and Design, 2008, "Predicting the geometric form of clad in laser cladding by powder using multiple regression analysis (MRA)," Materials & Design, 29(2), pp. 554-557.doi:10.1016/j.matdes.2007.01.023

[18] Ancona, A., Spagnolo, V., Lugara, P. M., and Ferrara, M., 2001, "Optical sensor for real-time monitoring of CO_2 laser welding process," Applied Optics, 40(33), pp. 6019-6025.doi:10.1364/AO.40.006019

[19] Song, L., Huang, W., Han, X., and Mazumder, J., 2017, "Real-Time Composition Monitoring Using Support Vector Regression of Laser-Induced Plasma for Laser Additive Manufacturing," IEEE Transactions on Industrial Electronics, 64(1), pp. 633-642.doi:10.1109/TIE.2016.2608318

[20] Song, L., and Mazumder, J., 2012, "Real time Cr measurement using optical emission spectroscopy during direct metal deposition process," IEEE Sensors, 12(5), pp. 958-964.doi:10.1109/JSEN.2011.2162316

[21] Nassar, A., Spurgeon, T., and Reutzel, E., 2014, "Sensing defects during directed-energy additive manufacturing of metal parts using optical emissions spectroscopy," Solid Freeform Fabrication Symposium Proceedings,

[22] Song, L., Wang, C., and Mazumder, J., 2012, "Identification of phase transformation using optical emission spectroscopy for direct metal deposition process," SPIE LASE, pp. 82390G-82390G-82399

[23] Khanzadeh, M., Chowdhury, S., Marufuzzaman, M., Tschopp, M. A., and Bian, L., 2018, "Porosity prediction: Supervised-learning of thermal history for direct laser deposition," Journal of manufacturing systems, 47, pp. 69-82

[24] Khanzadeh, M., Chowdhury, S., Tschopp, M. A., Doude, H. R., Marufuzzaman, M., and Bian, L., 2017, "In-situ monitoring of melt pool images for porosity prediction in directed energy deposition processes," IISE Transactions, pp. 1-19.doi:10.1080/24725854.2017.1417656

[25] Samatova, N. F., Hendrix, W., Jenkins, J., Padmanabhan, K., and Chakraborty, A., 2013, Practical graph mining with R, CRC Press.

[26] Sandryhaila, A., and Moura, J. M., 2014, "Big data analysis with signal processing on graphs: Representation and processing of massive data sets with irregular structure," IEEE Signal Processing Magazine, 31(5), pp. 80-90

[27] Suplee, C., 2009, "Atomic Spectra Database NIST, (2009)."

[28] Dunbar, A. J., and Nassar, A. R., 2018, "Assessment of optical emission analysis for in-process monitoring of powder bed fusion additive manufacturing," Virtual and Physical Prototyping, 13(1), pp. 14-19.doi:10.1080/17452759.2017.1392683

[29] Nassar, A., Starr, B., and Reutzel, E., 2015, "Process monitoring of directed-energy deposition of Inconel-718 via plume imaging," Solid Freeform Fabrication Symposium, Austin, TX, pp. 284-294

[30] Montazeri, M., and Rao, P., 2018, "Sensor-Based Build Condition Monitoring in Laser Powder Bed Fusion Additive Manufacturing Process Using a Spectral Graph Theoretic Approach," ASME Transactions, Journal of Manufacturing Science and Engineering, 140(9), pp. 091002-091002-091016.doi:10.1115/1.4040264

[31] Montazeri, M., Yavari, R., Rao, P., and Boulware, P., 2018, "In-Process Monitoring of Material Cross-Contamination Defects in Laser Powder Bed Fusion," Journal of Manufacturing Science and Engineering, 140(11), pp. 111001-111001-111019.doi:10.1115/1.4040543

[32] Cortes, C., and Vapnik, V., 1995, "Support-vector networks," Machine learning, 20(3), pp. 273-297

[33] Abdi, H., and Williams, L. J., 2010, "Principal component analysis," Wiley interdisciplinary reviews: computational statistics, 2(4), pp. 433-459